Journal of Applied Geophysics 65 (2008) 10–20

Contents lists available at ScienceDirect

Journal of Applied Geophysics

journal homepage: www.elsevier.com/locate/jappgeo

A resolution study of buried valleys using laterally constrained inversion of TEM data

Esben Auken *, Anders V. Christiansen, Lars H. Jacobsen [1], Kurt I. Sørensen

The Hydrogeophysics Group, Department of Earth Sciences, Høegh-Guldbergs Gade 2, 8000 Aarhus C, University of Aarhus, Denmark

ARTICLE INFO

Article history:
Received 11 April 2007
Accepted 10 March 2008

Keyword:
LCI
SkyTEM
TEM
Buried valleys
Paleo channels
Inversion

ABSTRACT

In this paper we present a study where the 1D laterally constrained inversion (1D-LCI) algorithm is used to invert continuously sampled synthetic 2D TEM data sets with 3D near-surface resistivity variation. The models are intended to closely resample typical hydrogeological targets such as paleo-channels or buried valley structures. In many parts of the world, these structures carry significant groundwater resources, or they can be associated with mineral deposits. Generating synthetic responses over known targets is an efficient to quantify how well a model is recovered by a combination of the applied geophysical method and the inversion algorithm. The 1D-LCI algorithm gives quasi 2D images of the subsurface efficiently suppressing 3D effects and the effect of data noise. Furthermore, layers with little signature in the data become resolved because the LCI algorithm distributes laterally the information. Based on the inversion of the synthetic 2D data sets we have constructed a robust setup of the inversion algorithm in terms of strength of the laterally constraints and regularization. This setup is used to invert measured data sets from a SkyTEM survey carried out over a buried valley structure.

1. Introduction

The transient electromagnetic (TEM) method is an induction method by which an electric current is induced into the ground from a high-powered transmitter loop. The size of the transmitter loop for groundbased systems can be in the order of 40×40 m^2 up to more than 200×200 m^2. When the transmitter has build up a steady current in the loop, the current is abruptly turned off, by which – due to Faraday induction – new currents are induced into the ground. It is the decaying magnetic field from these currents that is measured in an induction coil at the surface of the ground. As the method does not need any galvanic contact with the ground it can efficiently be applied on the ground or from airborne platforms.

The TEM method has been used worldwide for hydrogeological surveys since Fitterman and Stewart (1986) undertook a theoretical study on the applicability of the method for groundwater investigation. It is a fast and relatively cheap method for exploring the subsurface. The method yields high resolution of layers with low-resistivity making it suitable for delineation of high-resistivity aquifers bound by heavy clays, or for mapping fresh water–salt water interfaces (e.g. Meju et al., 1999; Dugue et al., 2008).

During the last decade new and enhanced helicopter-borne TEM systems have been developed. These systems not only increased the data volume significantly, but also gave so far unseen resolution capabilities of the subsurface. In some systems the data quality is comparable to that of similar data from groundbased systems and therefore calls for application of quantitative modeling and inversion algorithms. We maintain that the speed of processing and inversion is not as important as stability and the capability to extract maximum information about the subsurface resistivity structures from the data. Preferably, the inversion algorithm should benefit from the dense spatial data distribution obtained from the helicopter systems. This is possible if a traditional inversion scheme of single-site data sets is expanded to simultaneously inverting a large number of data sets along a profile thereby creating pseudo-2D images using a 1D based forward solution. An example of such an algorithm is the 1D laterally constrained inversion (1D-LCI) by Auken et al. (2005). Santos (2004) has published a similar algorithm for EM34 data.

A number of approaches for the 3D forward modeling of time domain EM response have been presented in the literature by e.g. Arnason (1995), Best et al. (1995), Alumbaugh et al. (1996) and Sugeng (1998). Full 3D inversion of TEM data is more rare. However, algorithms have been presented by e.g. Alumbaugh and Newman (2000) and Haber et al. (2004). Even though these studies show that 3D inversion of TEM data is possible, the computation power involved is significant, and presently efficient use of the algorithms requires access to small computer clusters. Multi-source data as airborne TEM data are even more challenging because the electric fields in the subsurface have to be solved for each source position.

* Corresponding author.
E-mail addresses: esben.auken@geo.au.dk (E. Auken), anders.vest@geo.au.dk (A.V. Christiansen).
URL: http://www.hgg.au.dk (E. Auken).
[1] Currently at Orbicon Inc, Viby, Denmark.

0926-9851/$ – see front matter © 2008 Elsevier B.V. All rights reserved.
doi:10.1016/j.jappgeo.2008.03.003

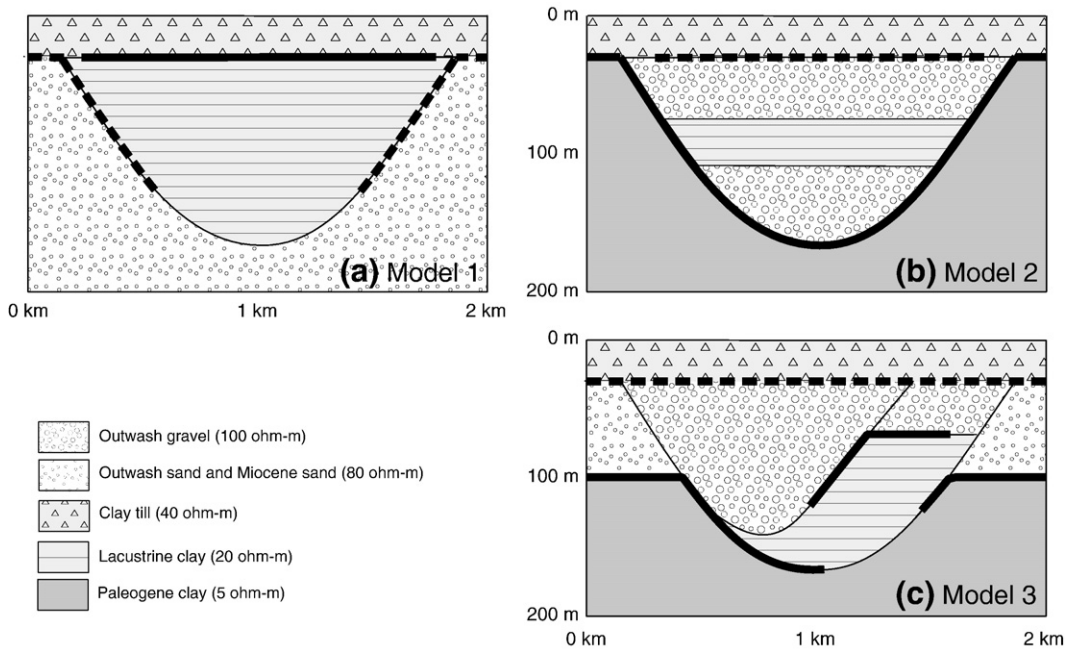

Fig. 1. Geological background for the synthetic 2D models. Modified from Jørgensen et al. (2003).

At present state, inversion of TEM data in a 3D environment is possible using a 1D forward solution. During the years, a number of papers have dealt with the effect of 3D structures in 1D interpretation of TEM data, e.g. Newmann et al, (1987), Goldman et al. (1994), Auken, (1995) and Hördt and Scholl, (2004). In general, these studies show that, if the geological environment consists of gently varying 3D structures with moderate resistivity contrasts, the 1D inversion approach in many cases gives a good recovery of the true model. In environments with high-resistivity contracts and strong 3D features a 1D based inversion algorithm is strongly influenced by 3D effects and will in many cases provide unreliable models.

In the following an inversion algorithm is used enabling production of pseudo 2D images in a moderate 3D environment, which resembles many hydrogeological sedimentary environments. The modeled data are based on synthetic 2D models with strong 3D near-surface resistivity variations contaminated by noise. The pros and cons of using the 1D-LCI algorithm are explored, and the experiences gained are used to invert a short profile of SkyTEM data.

2. Methodology

In the following we will describe the steps involved in the investigation, i.e.: 1) selection of the geological models, 2) calculation of the 2D forward data, 3) addition of noise to make data appear as field data, 4) inversion and 5) a final analysis of inversion results. In the following we discuss these steps.

2.1. The investigated geological models

The presented geological models are chosen from Jørgensen et al. (2003). They represent typical glacial geological models often referred to as buried valleys (see sketch in Fig. 1). Buried Quaternary valleys are complex structures filled with various deposits consisting primarily of glacio-lacustrine clay, till and meltwater sand and gravel. The valleys are important hydrogeophysical targets, because they often represent significant aquifers used for public water supply. The ability to map the valleys depends primarily on valley geometry, infill structure and the resistivity of the fill sediments and the substratum.

In all cases, the base model is a valley incised in either a homogeneous or a layered half-space, and the flanks of the valleys are sloping 26° reaching the bottom at a depth of 150 m. The top-layer is

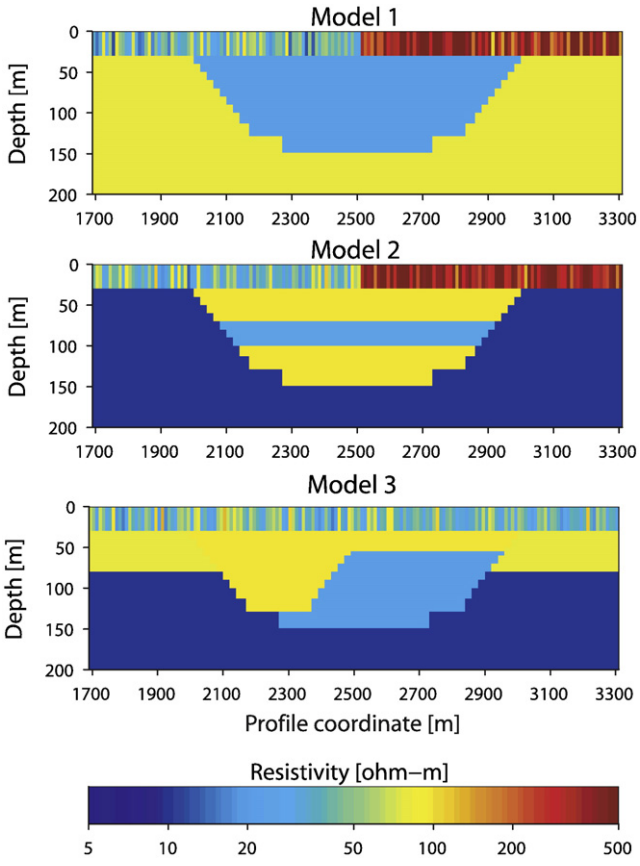

Fig. 2. The simplified 2D/3D models from Fig. 1 with lithology converted into resistivity. The overall model is 2D while the near-surface layer is 3D in order to simulate the effect of an inhomogeneous top-layer.

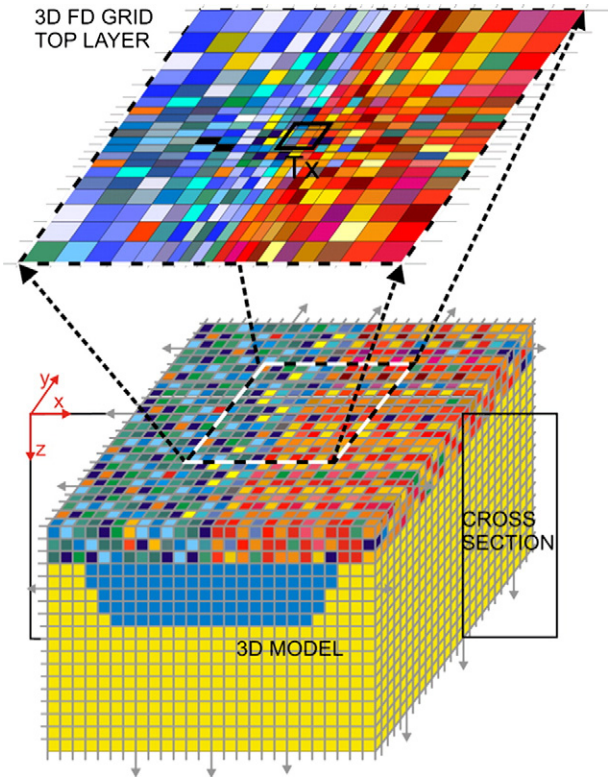

Fig. 3. a) Sketch of the 3D model grid with cells of 10×10×10 m. b) Sketch of the 3D FD grid where the resistivity of each cell is a volume weighted logarithmic average of the conductivities of the corresponding cells in the model grid. The loop at the center of the grid illustrates the transmitter.

30 m thick. The first model (Fig. 1a) represents a valley carved into Miocene sand with medium to high-resistivity of 80 ohm-m, filled entirely with glacio-lacustrine clay (20 ohm-m) and covered with clay till (10 ohm-m). Fig. 1b shows a simple model of a valley incised into a good conductor of Paleogene clay. The resistivity of the Paleogene clay is 5 ohm-m. The valley is filled with meltwater gravel of 100 ohm-m with an internal thin layer of glacio-lacustrine clay (20 ohm-m) and covered by clay rich till of 40 ohm-m. The last model in Fig. 1c represents also a younger valley filled with meltwater gravel cut into an older one filled with glacio-lacustrine clay in the lowest sections and meltwater gravel in the uppermost sections. The old valley is incised into Paleogene clay and Miocene sand, and the entire structure is covered by clay till.

2.2. 3D forward modeling and model description

To carry out the modeling, the geological sketches in Fig. 1 are turned into simplified 3D models with the lithology translated to electrical resistivities. Apart from the top-layer, the model is a 2D structure. Thus, the valley structures extend to infinity in both directions perpendicular to the profile section. Fig. 2 shows schematically a cross section for the models in Fig. 1.

To simulate the effect of an inhomogeneous top-layer (the first layer Fig. 2), the resistivities of the top-layer cells are calculated using a Gaussian distribution of the logarithm of the mean layer resistivity. The mean of the Gaussian distribution is 40 ohm-m at left sides and 400 ohm-m at right sides of the profiles (except for model 3 which has the 40 ohm-m layer through the entire section length). Also, the top-layer has an abrupt change in resistivities in the centre of the profile, which has three purposes: 1) to simulate a strong near-surface 2D effect and 2) to generate two different models with the same base model and 3) to exercise the capabilities of the inversion algorithm.

The forward responses were calculated using the code of Árnason (1995). The code solves for the electric and the magnetic fields on a 3D finite difference (3D FD) grid using spectral Lanczos decomposition for solving the matrix equation. The code calculates the impulse response from a rectangular loop located on the surface of the model.

Due to numerical considerations the 3D FD grid cannot enlarge sufficiently to describe the entire geological model shown in Fig. 2. Therefore, the geological model is discretized in what is called a model grid consisting of cubes with a side length of 10 m and each cube assigned a resistivity according to the model, as illustrated in the bottom of Fig. 3. To calculate the 3D response at a specific location in the model grid, the 3D FD grid is superimposed on the model grid (Fig. 3, top). The resistivity of each cell in the 3D FD grid is then calculated as a volume weighted logarithmic average of the conductivities in the implied model grid cells (Jacobsen, 2004). Simplified 2D resistivity models for presentation are obtained from each 3D model by cutting a vertical cross section at position $y=0$ (also illustrated in Fig. 3.).

In detail, the 3D FD grid has a fine central part containing the model, the transmitter and receivers as well as padding zones both laterally and vertically (Fig. 3). The grid has 53×53 nodes in the x–y plane and 40 nodes in the z-plane (a total of 112,360 nodes). In a 160×160 m center of the grid, the node distance in the x–y plane is 10 m. Outside this area, the nodes are distributed by 10 nodes per decade. In the z-direction the upper 10 nodes are linearly distributed with spacing 10 m and below that with 10 nodes per decade. The total size of the grid is approx. 6200×6200×3100 m. The grid dimensions yield accurate data from about 8 μs to 2–4 ms.

Numerous experiments with the setup of the grid are described in Toft (2001). He also tested the finite difference code against the models in Auken (1995) which were calculated using the integral equation code of Wannamaker et al. (1984). He finds that the responses using a 3D grid like the one described above differ less than 10% at all times.

2.3. LCI inversion

The laterally constrained inversion scheme is described in detail in Auken and Christiansen (2004). The model is represented by stitched-together 1D models along a section of a profile as outlines in Fig. 4. The lateral distances between the 1D models are determined by the sampling density of data and may be non-equidistant. The model parameters are layer resistivities and thicknesses, and the data are time-series of the time-derivative of the magnetic field measured at the sounding positions.

For the practical field application, the data sets have to be divided into sections with typically up to 1000 model parameters. In the

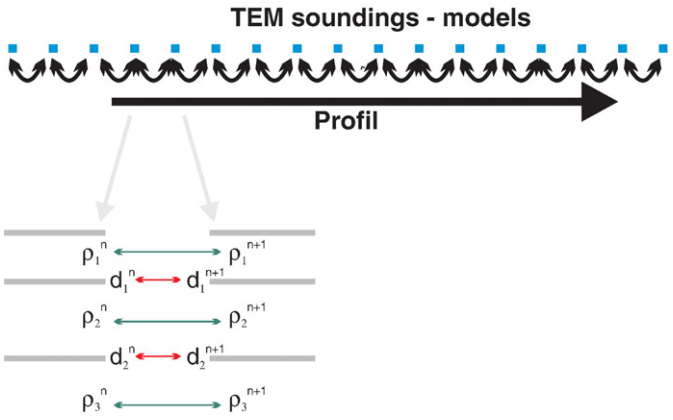

Fig. 4. The laterally constrained inversion model setup. Each sounding along the profile has an associated model. The model parameters, layer resistivities and thicknesses/depth are constrained so that parameters in neighboring models have to be equal within certain limits.

synthetic part of this study, all data sets are inverted simultaneously, minimizing a common objective function including the lateral constraints. Consequently, the output models form a balance between the constraints, the physics of the method and the data. Model parameters with little influence on data will be controlled by the constraints and vice versa. Due to the lateral constraints, information from one model will diffuse to neighbouring models. The lateral constraints can be considered as a priori information on the geological variability (within the partly overlapping sensitivity volumes of the measurements). The smaller the expected variation for a model parameter is, the tighter the constraint should be. The resulting model is laterally smooth with sharp layer interfaces. In practice the number of free parameters in the inversion is reduced because of the assumption that geological coherence is represented by the lateral constraints. The implementation of the LCI algorithm also allows adding geological a priori information on any of the model parameters — resistivities, thicknesses or depth to interfaces.

The 1D-LCI algorithm was originally developed for resistivity data (Auken et al, 2005), for which it efficiently suppresses static effects and to some extent decreases the number of equivalent modellayers. The algorithm minimizes the object function using the L2-norm. Furthermore, due to the lateral constraints, the 1D-LCI resistivity algorithm is robust to 2D earth structures. TEM data do not suffer from static effects, and for the central loop configuration the method is relatively insensitive to lateral resistivity variations. The main expected outcome of the 1D-LCI is therefore an enhanced model resolution in the deepest parts of the model corresponding to late decay times.

The laterally constrained inversion is an over-determined problem. Therefore, a sensitivity analysis for the model parameters can be calculated. This is essential for assessing the resolution of the output model (Tarantola and Valette, 1982) and evaluating the integrity of the model.

Because the model parameters are represented as logarithms, the analyses provide a standard deviation factor (STDF) of the parameter (equation 11 in Auken et al., 2005). The STDF corresponds to the standard deviation in log space of the model parameter. As the theoretical case of perfect resolution has a STDF=1, a factor of STDF=1.1 is approximately equivalent to an error of 10%. We consider that well resolved parameters have a STDF<1.2, moderately resolved parameters within 1.2<STDF<1.5, and poorly resolved parameters within 1.5<STDF<2, and that unresolved parameters have a STDF>2.

2.4. Natural noise contribution and data processing

To obtain realistic results we try to imitate the characteristics of field data as close by as possible. The transient data value for a given time gate is an averaging of the induced electromotive force in the receiver coil within the gate interval. Ground-based methods normally use logarithmic gating, implying that the length of a gate is proportional to the delay time. If the surrounding noise is white (i.e., stochastic and with same power through all frequencies), logarithmic gating results in an average noise decay proportional to $t^{-1/2}$ (Munkholm and Auken, 1996). However, the noise spectrum is not completely white, as it is often dominated by AM radio transmitters with high coherent peaks at single frequencies. This overlays the white noise and averaging and stacking result in an effective noise decay of t^{-1} (Christiansen and Christensen, 2003). The noise from radio transmitters dominates at early times, whereas the stochastic noise dominates at late times. The total noise is the sum of both contributions.

In sedimentary environments with relatively high signal levels, the t^{-1} noise can be neglected leaving:

$$V_{\text{resp}} = V + G(0,1)\cdot\left[\text{STD}_{\text{uni}}^2 + \left(\frac{V_{\text{noise}}}{V}\right)^2\right]^{\frac{1}{2}}\cdot V, \quad (1)$$

where V_{resp} is the perturbed synthetic data, V is the synthetic noiseless data, $G(0,1)$ is the Gaussian distribution with zero mean and standard deviation 1, $\text{STD}_{\text{uni}}^2$ is the uniform noise, and V_{noise} is the background noise contribution. V_{noise} is given by

$$V_{\text{noise}} = b\cdot\left(\frac{t}{1\cdot 10^{-3}}\right)^{-\frac{1}{2}}, \quad (2)$$

where b is the noise level at 1 ms. Our experience shows that, in many parts of the world, this number ranges between 1 nV/m^2 to 5 nV/m^2 with a stack size of 1000 transients. The uniform standard deviation accounts for instrument and other non-specified noise contributions. It is typically set to 2% for db/dt responses.

Fig. 5 shows an example of the effect of noise perturbation with the noise model described in Eq. (1). The lower curve assumes a transmitter moment of 4800 Am^2 corresponding to a current of 3 A transmitted in a 40×40 m^2 loop. The effect of the noise perturbation is obvious, especially around 1 ms, where the transition between noiseless data and noise dominated data occurs. The effect of increasing the transmitter moment by a factor of 25 is seen on the upper curve. In this case the transition from noiseless to noise dominated data occurs around 7 ms.

After noise perturbation data were processed as if they were field data. This includes an automatic removal of the noisiest data points, followed by a visual inspection checking the outcome of the automatic procedure.

2.5. 1D forward modeling

The synthetic data are true impulse responses and therefore not influenced by the effect of transmitter turn-off ramps and low-pass filters in the receiver system (also called the system response). For the field data example, these effects are modeled in the forward code and not by deconvolution of the measured data sets. Our experience shows that deconvolution of system parameters in the data sets tends to be an unstable process. Our forward modeling algorithm (based on Ward

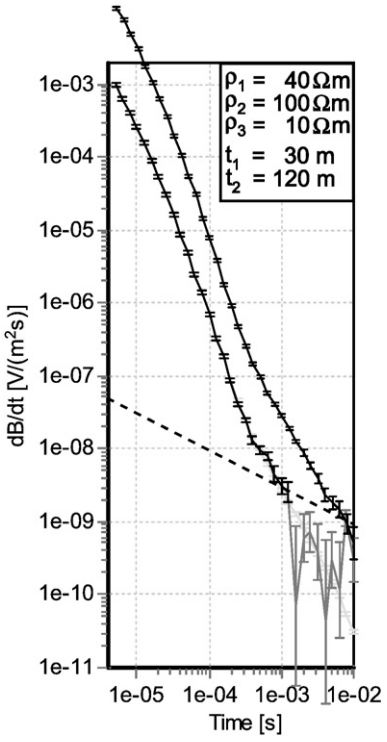

Fig. 5. Noise perturbation. Unperturbed forward response from the model, shown in the upper right corner, is marked light grey. Perturbed data are dark grey and black. An average noise level of 3 nV/m2 at 1 ms (illustrated by the straight line) is assumed. The uniform noise contribution is 2%. The lower data curve is for a transmitter moment of 4800 Am^2 while the moment for the upper curve is increased by a factor of 25.

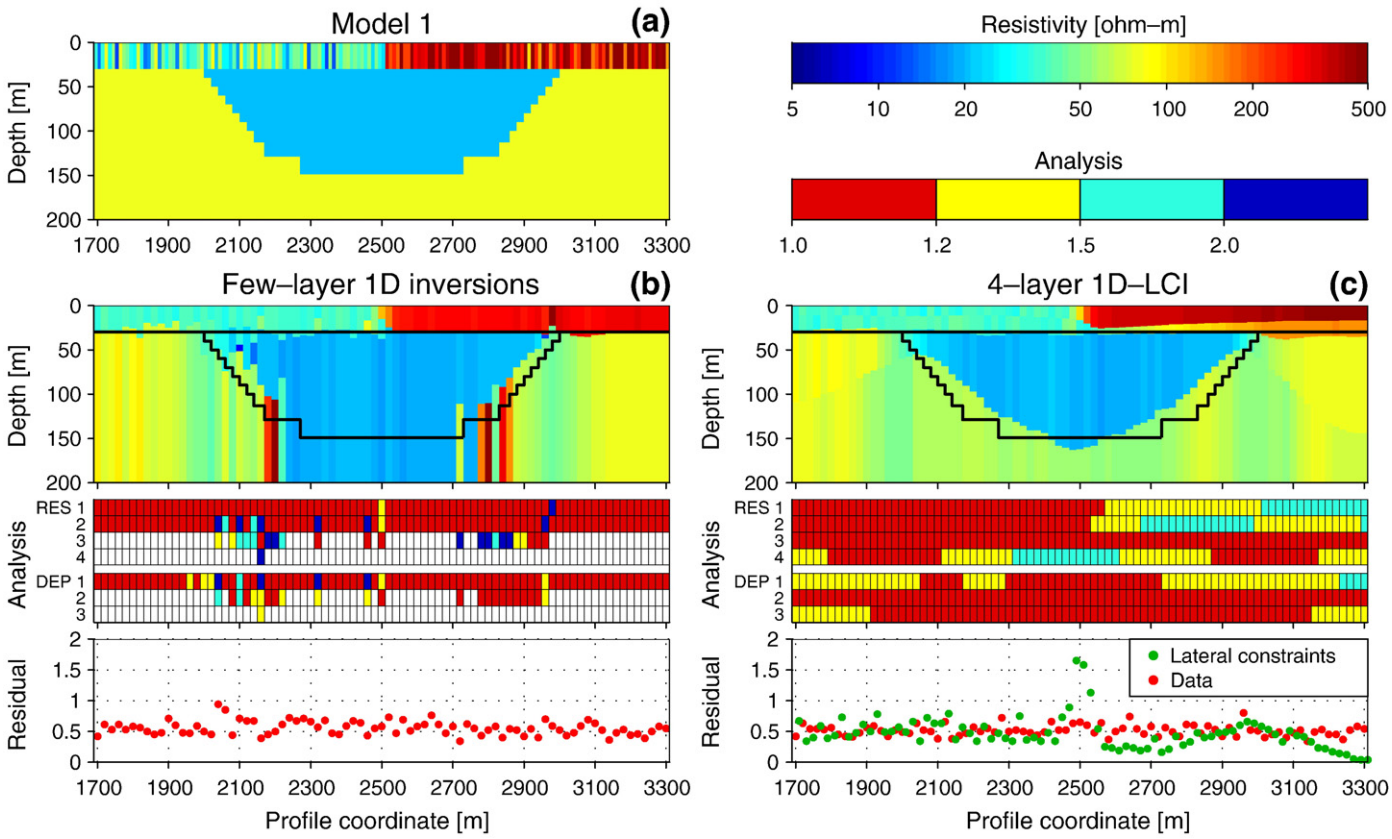

Fig. 6. Panel (a) is a profile in the center part of the true model 1. Panel (b) is a section of stitched-together few-layer inversions with the analyses and data residuals plotted below. Panel (c) is the four-layer LCI-section with the analyses and residuals for lateral constraints and data plotted below. The analyses use a four-graded color code ranging from red (well determined) to blue (undetermined).

and Hohmann, 1988) includes modeling of low-pass filters (Effersø et al., 1999) and the turn-on and turn-off ramps (Fitterman and Anderson, 1987). For field data the errors are estimated from the data stack.

3. Synthetic examples

The following is a presentation of inversion results of the models shown in Fig. 2. For each model we applied a few-layer single-site inversion and a laterally constrained inversion, LCI. The output of the few-layer inversion is defined by the model with the smallest number of layers fitting the data to a satisfactory level. This is evaluated for each data set on the profile and afterwards stitched together to one pseudo 2D image. The LCI method takes in all data sets and models in one batch and has the same number of layers along the profile. The number of layers is determined as the maximum number of layers used in the few-layer single-site inversion.

Set-up of the lateral constraints requires consideration of the sampling density along the profile. The constraints between the models are based on 1) every TEM resistivity model being constrained to its nearest models in both directions and 2) the lateral constraint for parameter n, C_l^n, being scaled according to the model separation, d, using a pragmatic power law formulation.

$$C_l^n = \left(C_r^n - 1\right)\left(\frac{d}{d_r}\right)^p + 1 \tag{3}$$

where C_r^n is a reference constraint, which is a function of some reference distance, d_r. Therefore, if the distance between two constrained models is twice that of the reference distance, the constraint values between the two models are multiplied by a factor of 2^p. In this study, p was set to 0.5 by trial-and-error achieving a subsurface image with sufficient complexity while maintaining laterally coherent layers.

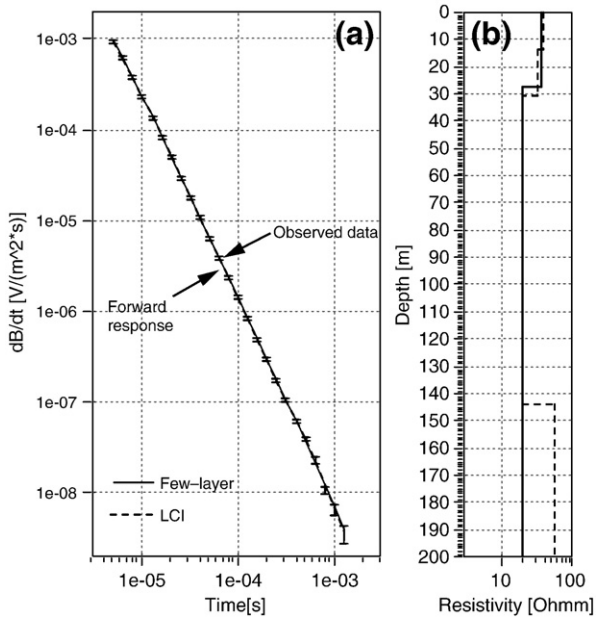

Fig. 7. In (a) model responses from 1D models at coordinate 2400 m are shown, according to the models plotted in (b). The stitched-together few-layer model and response are shown with the solid line, the LCI model and response are shown with the dashed line.

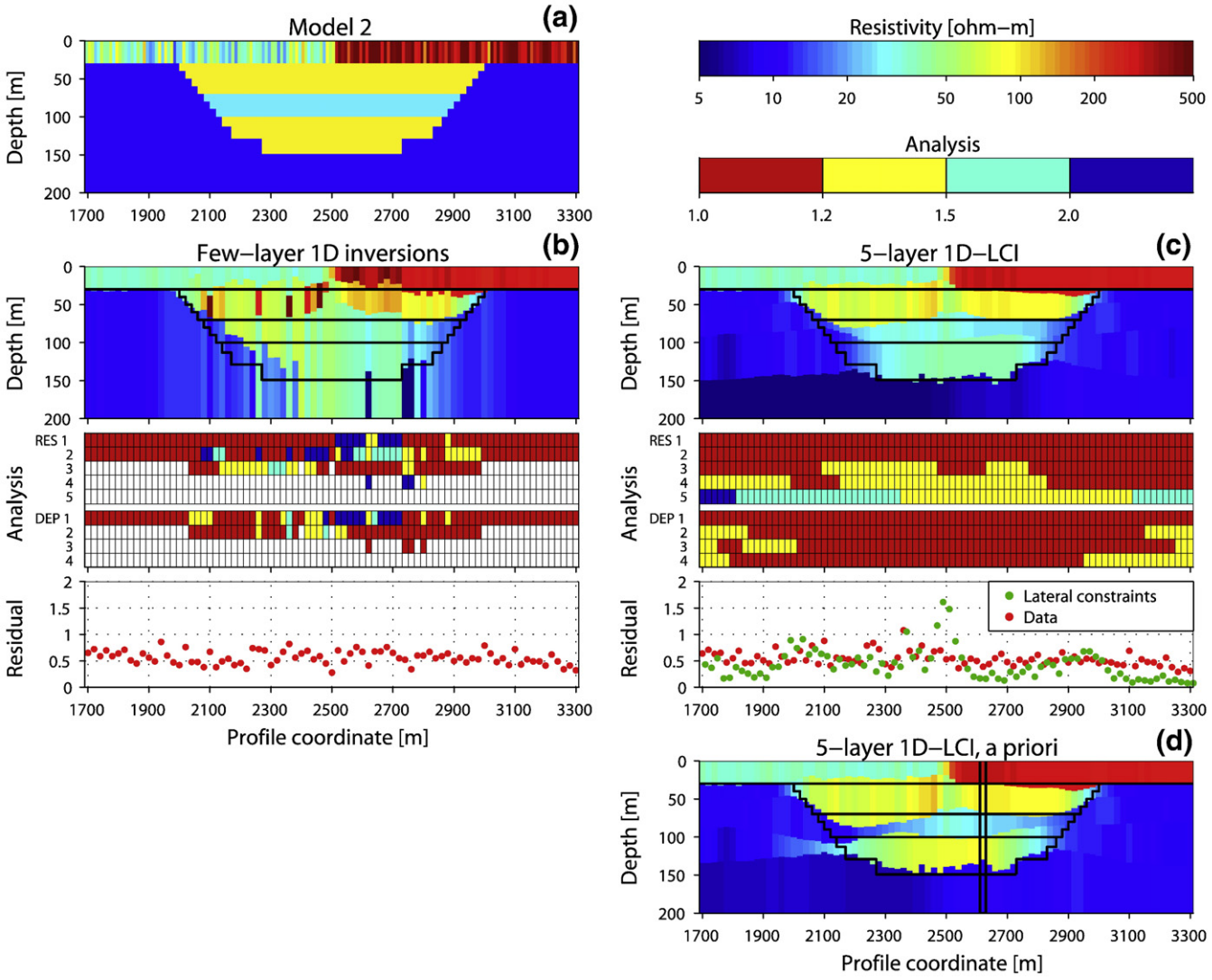

Fig. 8. Panel (a) is a profile in the center part of the true model 2. Panel (b) is a section of stitched-together few-layer inversions with the analyses and data residuals plotted below. Panel (c) is the 5-layer LCI-section with the analyses and residuals for lateral constraints and data plotted below. Panel (d) is similar to (c) except that a priori information about the resistivity of the lower high-resistive layer is added to the inversion.

In all cases the starting model is a half-space with a uniform resistivity of 50 ohm-m. The layer thicknesses of the starting model were logarithmically distributed. Care was taken that no layer boundary in the starting model was equal to a layer boundary in the 2D model. Inversions were calculated with four or five layers. The five-layer model was only picked for presentation if the data residual for that model was significantly lower than the residual for the four-layer model. It has to be emphasised, though, that in all cases the five-layer model gave similar results as the four-layer model as the inversion algorithm tends to end up with two consecutive layers with about the same resistivity if the model has to many layers.

The lateral constraints can be applied on thicknesses as well as depths. Constraints on depths favour horizontal layer boundaries whereas constraints on thicknesses favour constant thickness in layers. For this case, we have used lateral constraints on depths. Constraints are relative for both resistivities and depths. We used reference constraints, C_r^n, of 1.2 on all the resistivities and 1.1 on all depths. The reference distance, d_r, is 20 m, reflecting the sounding distance for the synthetic examples. This means that models are allowed to vary approximately 20% in resistivities and 10% in depths over 20 m in average.

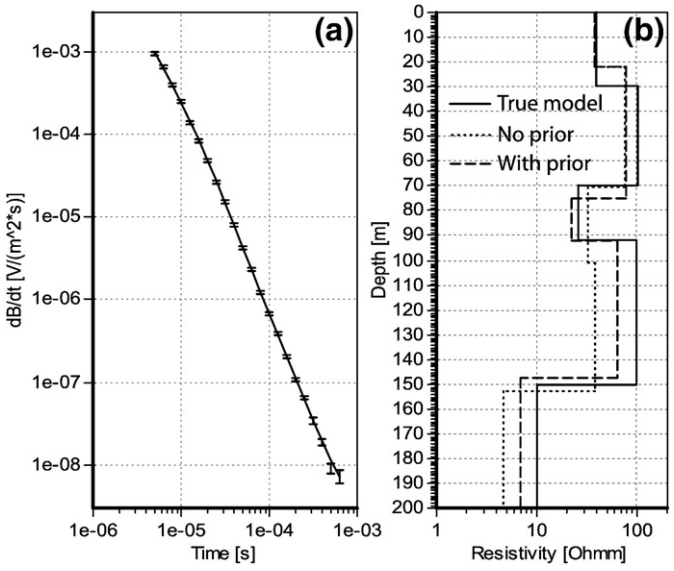

Fig. 9. In (a) model responses from 1D models at coordinate 2400 m are shown, according to the models plotted in (b).

3.1. Model 1 — simple incised valley

The first synthetic model shown in Fig. 6a is a simple incised valley with a varying cover layer.

The few-layer stitched-together model section is presented in Fig. 6b. The top-layer is well resolved in both sides, with mean resistivities reflecting the mean resistivities of the layer. The resistivity change in the central part is also resolved, with only an indication of associated 2D effects. On the flanks of the valley, the high-resistive bottom layer is resolved, but in the central part, for depths larger than 130 m, the bottom layer cannot be resolved. The parameter analyses reflect mainly well determined parameters whenever the model has only two layers and a somewhat poorer determination of the three- and four-layer models. The data residuals are in all cases well below one, indicating that data are fitted within the observation error.

A four-layer LCI model is shown in Fig. 6c. The most pronounced difference compared to the few-layer inversion is the resolution of the depth of the valley for the entire profile. The lateral constraints draw information on the layer boundaries and layer resistivities to the centre of the profile, where only limited information of the depth to the bottom of the valley is available. The analyses present well to moderately-well determined parameters. The depth to the bottom of the valley is well determined taking advantage of the information coming from the lateral constraints. The data residuals of the lateral constraints are well below one, except for the central part where the lateral constraints are "stressed" due to the rapid resistivity changes in the first layer required by the data.

Fig. 7 shows plotted data and models from coordinate 2400. Obviously there is little evidence in the data about the bottom layer at this position as reflected in the few-layer inversions. However, including the lateral constraints restricting the geological variation we see that the resulting model closely resembles that of the true 1D model at that site. The underestimated depth to the bottom layer is most likely explained by 2D effects from the sides of the valley causing the signal to be too low at late times.

3.2. Model 2 — low-resistive layer

The valley model in Fig. 8a is incised in a low-resistivity background with a high-resistivity fill containing a low-resistivity layer.

The few-layer stitched-together model section is presented in Fig. 8b. Similar to the analysis of model 1, the top-layer is well resolved

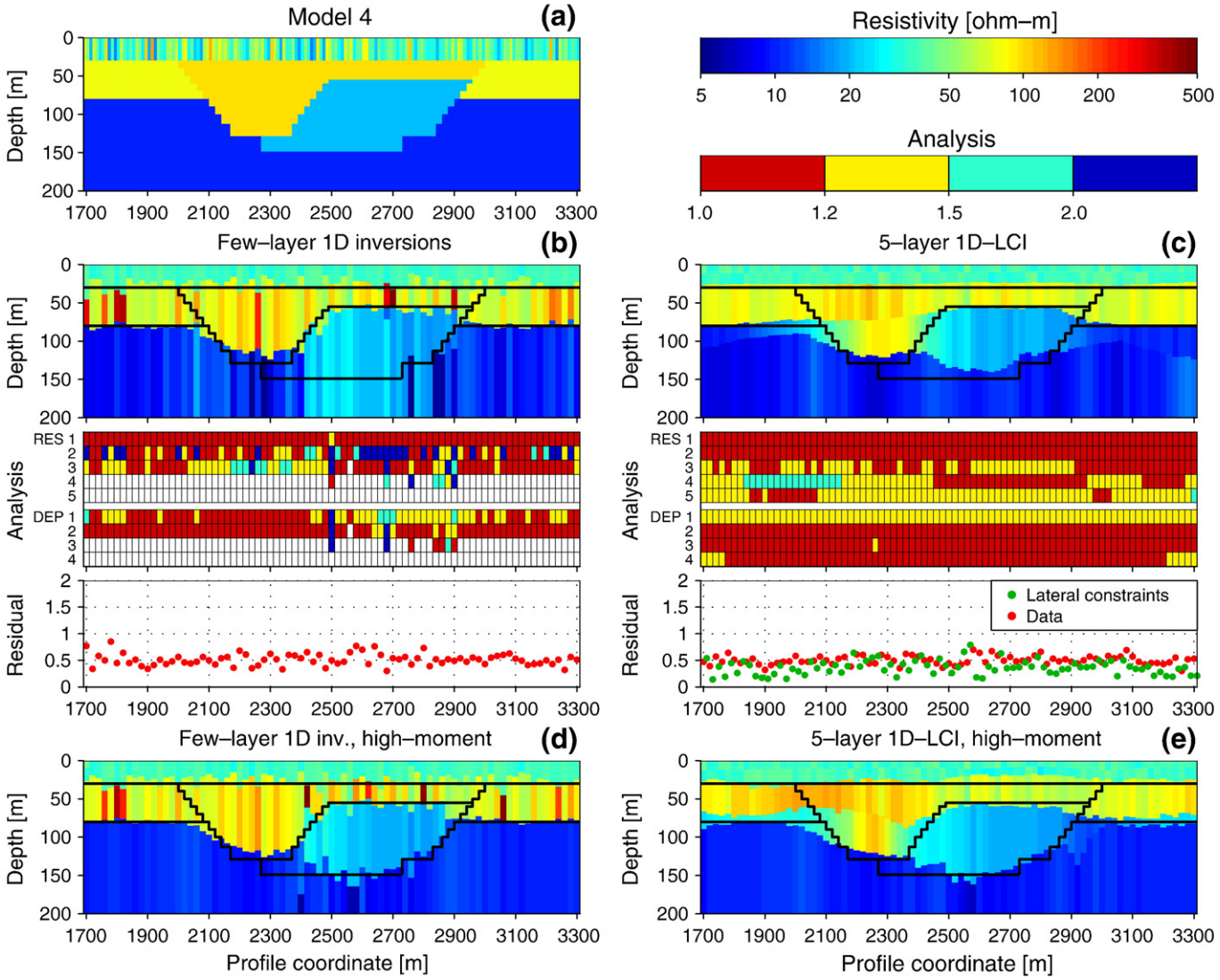

Fig. 10. Panel (a) is a profile in the center part of the true model 4. Panel (b) is a section of stitched-together few-layer inversions with the analyses and data residuals plotted below. Panel (c) is the 5-layer LCI-section with the analyses and residuals for lateral constraints and data plotted below. Panel (d) is a section of stitched-together few-layer inversions with the magnetic moment increased to 50,000 Am^2. Panel (e) is the 5-layer LCI-section obtained with the high-moment data. The analyses use a 4-graded color code ranging from red (well determined) to blue (undetermined).

on both sides. The flanks of the low-resistivity valley floor are also well resolved, but in the central part the information on the depth of the valley floor is lost. The three layers filling the valley are not resolved. The top high-resistivity layer in the valley is resolved on the right side, but only partly resolved on the left side indicating strong equivalence and possibly 2D effects from the sharp transition in the top-layer. The low-resistivity layer and the bottom high-resistivity layer in the valley are combined to one layer with an intermediate resistivity. The reason for the left and right sides differing that much can be explained by "screening". A low-resistivity top-layer produces a high response at relatively later times compared to a high-resistivity layer. The weak response from the underlying high-resistivity layer drowns in this response and the resolution of the layer is partly lost. The model parameter analyses reflect mainly well determined parameters, and the data residuals are well below one.

A 5-layer LCI inversion is shown in Fig. 8c. In this section, the top high-resistivity layer of the valley fill is resolved. The screening of the second layer is not as pronounced as in the stitched-together section, but still indicated by slightly more shifted layer boundaries to the left side of the model compared to the right side. The bottom two layers of the valley fill are still not resolved, although some indication of a higher resistivity in the bottom is seen.

In order to investigate further the capabilities of the LCI method to detect poorly resolvable layers, we added a priori information to one sounding on the profile. The a priori information is intended to represent a drill hole in which we have detailed information on layer thicknesses and resistivities. The a priori drill hole information is added at coordinate 2620 and consists of information on layer boundaries and layer resistivities. The information is added with an uncertainty factor of 1.2 on resistivities and 1.1 on depths. The result of the LCI model with the a priori drill hole information added is seen in Fig. 8d. Compared to the model with no a priori drill hole information, it is now possible to distinguish the two bottom layers filling the valley. It is important to notice that the a priori drill information migrates from the point of insertion throughout the profile caused by the lateral constraints.

Fig. 9 shows plotted data and models from coordinate 2400 m. Even here, more than 200 m (11 soundings) away from the point where the a priori information was added, the model resolution clearly improved (Fig. 9b) although not clearly visible on the data fit (Fig. 9a).

3.3. Model 3 — 2D valley fill

The valley model in Fig. 10a represents a low-resistivity 2D-structure filling the right side of the valley floor.

The few-layer stitched-together model section is presented in Fig. 10b. The most striking feature is the lack of information on the depth extent of the low-resistivity 2D body at the right side of the valley. The parameter analyses reveal a mixture of well and poorly determined parameters except for the resistivity of the first layer which is well determined throughout.

The LCI-section in Fig. 10c enhances the resolution of the low-resistivity 2D body because the lateral constraints are able to extract

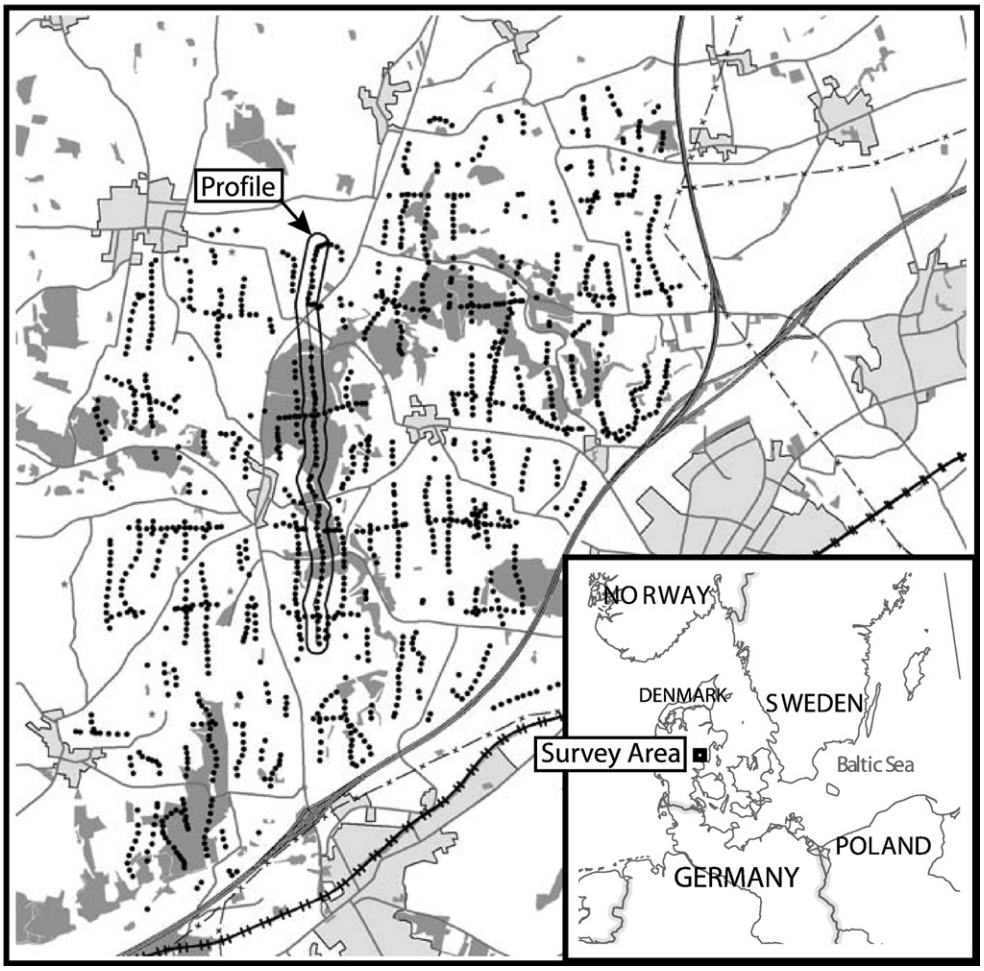

Fig. 11. The map shows the Stjær field area covering approximately 40 km^2. Each dot represents two soundings; a high- and a low-moment sounding. A total of 140 km of profile data were measured resulting in 1347 soundings combining a high- and a low-moment data set.

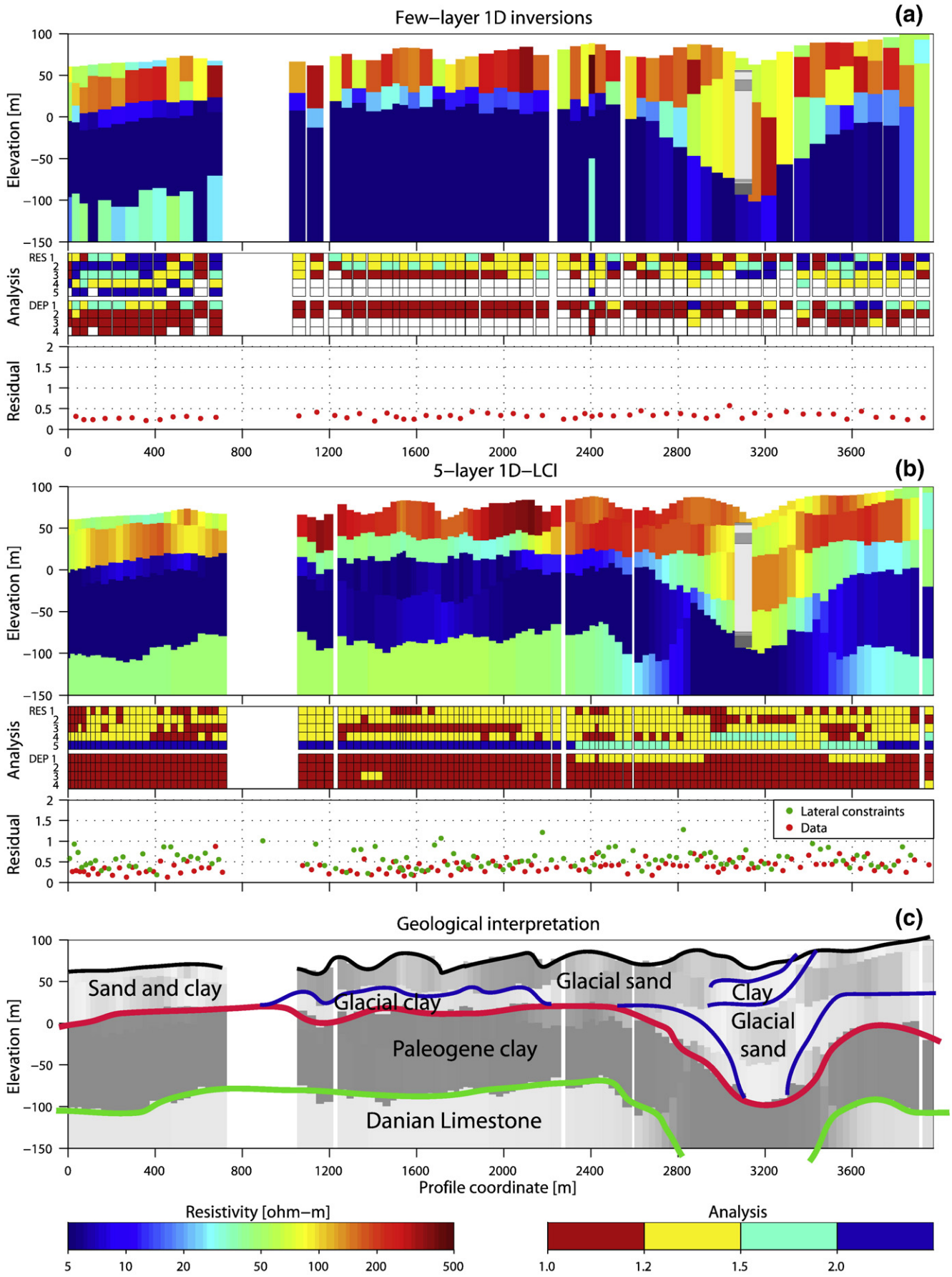

Fig. 12. Panel (a) is a section of stitched-together few-layer inversions with the analyses and data residuals plotted below. Panel (b) is the 4-layer LCI-section with the analyses and residuals for lateral constraints and data plotted below. The analyses use a four-graded color scale ranging from red (well determined) to blue (undetermined).

information from the sides underneath the bottom of the body. As a side effect the edges of the small side-valley around coordinate 2300 m are somewhat smoothed, but neither the data nor the lateral constraints show a significantly misfit indicating that the constraints are properly set.

In this case the determination of the low-resistivity 2D body, of course, depends heavily on the data quality. In Fig. 10d and e we have simulated the result obtained if the magnetic moment of the transmitter was 50,000 Am^2 instead of 4800 Am^2 (as used in all previous sections). Increasing the magnetic moment by a factor of ≈10 improves the S/N ratio, which results in more reliable data at late times. The penetration depth is enhanced by a factor of ≈1.6.

The results of the higher moment appear from Fig. 10d and e for the stitched-together section and the LCI-section, respectively. The effect of the increased moment is obvious in the stitched-together section where the extension of the low-resistive 2D body is now accurately delineated. The high-resistivity second layer is still influenced by equivalences resulting in rapid non true variations along the profile.

The data quality improved essentially at late times only and the low-moment data already contained sufficient information in that part to outline the main features. Therefore, the LCI-section (Fig. 10e) using the high-moment data reveals no important improvement compared to the result with the low-moment data (Fig. 10c).

4. Field example, SkyTEM survey, Denmark

In order to illustrate the applicability of the LCI algorithm to field data, we present a data set measured with the SkyTEM helicopter-borne system. More details about the system can be found in Sørensen and Auken (2004). Very briefly, the SkyTEM system produces data sets with high and low moments alternating along the profile. Data sets are separated by approx. 30–50 m depending on the flight speed. In the illustrated field example, the magnetic moment was 28,000 Am^2 for the high-moment and 4700 Am^2 for the low-moment. By experience we know that the penetration depth in the current geological environment is approximately 150 m. Currently (February 2008), the SkyTEM system has a maximum moment of 150,000 Am^2. To avoid alternating models along the profile, a normal 1D inversion of these data combines one low-moment with one high-moment sounding to produce just one model. In the LCI-concept the high-moment and low-moment soundings are treated as individual data sets, thus resulting in twice the number of models.

Data are presented here from the 40 km^2 Stjær survey shown in Fig. 11. Each black dot represents two soundings: a low- and a high-moment sounding. Average spacing between flight lines is 250 m. All soundings have been removed in a 100–150 m wide buffer zone around most roads because of transmitter induced couplings in power lines and cables buried on the roadsides (Danielsen et al., 2003).

In general terms, the geology of the survey area consists of Danien freshwater saturated limestone at the bottom, and, on top of this, 50–100 m heavy Paleogene clay with an average resistivity of 5 ohm-m. The upper 20–50 m consist of till with a varying clay content and glacial sands. It was expected that one or more buried valleys were incised into the Paleogene clay. These valleys are filled with outwash sand and gravel and represent important aquifer structures (Auken et al., 2003, Jørgensen et al., 2003).

The results of the data inversion are shown in Fig. 12. The white section in the profile reflects data that have been removed due to coupling to man-made conductors.

Panel (a) presents the stitched-together few-layer 1D inversions. The data sets are inverted using 2, 3, 4 or 5-layer models. The general appearance is a low-resistivity layer at depth with more resistive layers on top and with a pronounced valley structure at the right side of the profile. The depth to the bottom of the valley structure is confirmed by a drilling located on the left flank of the valley some 170 m away from the profile. To the left, a more resistive layer is seen below the low-resistivity layer. The top-layer displays mixed high and low resistivities indicating mixed glacial sediments. The low-resistivity layer has a fairly constant resistivity of 5 ohm-m with an undetermined thickness, except for the left part which is approximately 100 m thick. The bottom layer to the left appears to have moderate- to high-resistivity, but the resistivity is poorly determined as shown in the analyses below. This is most likely the Danian chalk found elsewhere in the area. The analyses reveal mainly well determined parameters for the top-layers, but only moderately to poorly determined parameters for the bottom layers. Data are well fit within a normalized residual of 1 all along the profile.

The LCI-section in Fig. 12b reveals the same overall characteristics as the stitched-together 1D inversions, but with a smoother and more continuous appearance. Applying the lateral constraints it is seen that the high-resistivity layer at depth is found for the entire profile except beneath the valley structure. Thus, the lateral constraints add sufficient information of the expected geological variability to extract from the data the sparse information of this layer. The analyses reveal well determined parameters except for the resistivity of the bottom layer which is undetermined. Note, however, that a high-resistivity layer at depth is needed to fit both the data and the lateral constraints, but we are unable to say anything about the resistivity other than *high*. The data and constraint residuals are fit mostly below a normalized residual of 1.

In panel (c) a geological interpretation has been drawn on top of the profile. Most interesting is the location of the valley and the apparently associated depression in the Danian chalk. The survey area is located at the southern flank of a salt diapir, which pushes the entire sequences upwards. It is known from other salt structures that the chalk sitting on the top and sides of the salt-structure is likely to be faulted. In this case it seems that pre-paleogene depression in the chalk gives a constant thickness of the clay package. The depression seen in the chalk actually migrates all the way to the surface on which a small valley is seen. The drilling was made based on the valley structure location foreseen by the SkyTEM investigation. Today the bore hole is used for extracting drinking water from the valley.

5. Discussion

The LCI algorithm is formulated in general concepts, i.e. it works equally well on different kinds of data sets along a profile as on the same data type along the profile. The latter is what is presented in this paper. Experiments with promising results have been performed with combined LCI inversion of DC and TEM data (Christiansen et al., 2007) as well as combined inversion of DC and surface wave dispersion data (Wisen and Christiansen, 2005). In these cases, the different sensitivities of the different physical parameters (resistivity, density, velocity, etc.) are combined to optimize the best layered model.

The LCI was originally developed for producing 2D models, but with a 1D forward solution. This was extended so the algorithm for DC data exists in a version where the forward solution is based on a 2D finite difference forward solution (Auken and Christiansen, 2004), producing layered 2D models. With a time-efficient 2D or 3D forward code for TEM data, a LCI algorithm could easily be implemented for TEM data as well.

6. Conclusion

We have shown that the 1D-LCI algorithm modified for inversion of densely sampled TEM data results in highly enhanced images of the subsurface resistivity structures. The algorithm has been thoroughly tested on a suite of typical models resembling 2D buried valley structures with a 3D varying overburden.

Comparison of single-site independent inversion with the LCI inversion shows that, in general, the LCI does not change well resolved parameters, whereas it improves the resolution of weakly resolved parameters, because information from neighboring soundings diffuses through the lateral constraints. In other words, “gaps” are not just

filled between the soundings, but the number of free parameters in the inversion is reduced because of the assumption that geological coherence is expressed by the lateral constraints. This was clearly demonstrated by both the synthetic examples and the field example where the surface of a limestone layer, buried under almost 100 m of tertiary clay with low-resistivity, was resolved by applying the LCI algorithm.

The presented study also illustrated that inversion of data measured over a 2D geological environment with moderate resistivity contrasts, using an algorithm based on a 1D forward solution, is quite robust and gives reliable images of the subsurface. Major features are well recognized whereas minor features, because of the diffusive nature of the subsurface currents, are to some extent smeared out.

Acknowledgements

We are grateful to the County of Aarhus for the permission to publish the field data and for the fruitful discussion with Verner Søndergaard, County of Aarhus (now GEUS), for the input to the geological interpretation. We would also like to thank Flemming Jørgensen, County of Vejle (now GEUS), for the numerous discussions on the validity of the output of the synthetic data from a geological point of view. Andrea Viezzoli and Niels B. Christensen gave valuable reviews before submission. Andreas Hördt (editor) and the two anonymous reviewers had valuable comments greatly clarifying parts of the paper.

References

Árnason, K., 1995. A consistent discretization of the electromagnetic field in conducting media and application to the TEM Problem. International Symposium on Three-Dimensional Electromagnetics, pp. 167–180.

Alumbaugh, D.L., Newman, G.A., 2000. Image appraisal for 2-D and 3-D electromagnetic inversion. Geophysics 65, 1455–1467.

Alumbaugh, D.L., Newman, G.A., Prevost, L., Shadid, J.N., 1996. Three-dimensional wideband electromagnetic modeling on massively parallel computers. Radio Science 31, 1–23.

Auken, E., 1995. 1D time domain electromagnetic interpretations over 2D and 3D structures. Proceedings of the Symposium on the Application of Geophysics to Engineering and Environmental Problems, Orlando, USA. EEGS, pp. 329–338.

Auken, E., Christiansen, A.V., 2004. Layered and laterally constrained 2D inversion of resistivity data. Geophysics 69, 752–761.

Auken, E., Jørgensen, F., Sørensen, K.I., 2003. Large-scale TEM investigation for groundwater. Exploration Geophysics 33, 188–194.

Auken, E., Christiansen, A.V., Jacobsen, B.H., Foged, N., Sørensen, K.I., 2005. Piecewise 1D laterally constrained inversion of resistivity data. Geophysical Prospecting 53, 497–506.

Best, M.E., Duncan, P., Jacobs, F.J., Scheen, W.L., 1995. Numerical modeling of the electromagnetic response of three-dimensional conductors in a layered earth. Geophysics 50, 665–676.

Christiansen, A.V., Christensen, N.B., 2003. A quantitative appraisal of airborne and ground-based transient electromagnetic (TEM) measurements in Denmark. Geophysics 68 (2), 523–534.

Christiansen, A.V., Auken, E., Foged, N., Sørensen, K.I., 2007. Mutually and laterally constrained inversion of CVES and TEM data — a case study. Near Surface Geophysics 5, 115–124.

Danielsen, J.E., Auken, E., Jørgensen, F., Søndergaard, V.H., Sørensen, K.I., 2003. The application of the transient electromagnetic method in hydrogeophysical surveys. Journal of Applied Geophysics 53, 181–198.

Duque, C., Calvache, M.L., Pedrera, A., Martín-Rosales, V.M., López-Chicano, M., 2008. Combined time domain electromagnetic soundings and gravimetry to determine marine intrusion in a detrital coastal aquifer (Southern Spain). Journal of Hydrology 349, 536–547.

Effersø, F., Auken, E., Sørensen, K.I., 1999. Inversion of band-limited TEM responses. Geophysical Prospecting 47, 551–564.

Fitterman, D.V., Anderson, W.L., 1987. Effect of transmitter turn-off time on transient soundings. Geoexploration 24, 131–146.

Fitterman, D.V., Stewart, M.T., 1986. Transient electromagnetic sounding for groundwater. Geophysics 51, 995–1005.

Goldman, M., Tabarovsky, L., Rabinovich, M., 1994. On the influence of 3-D structures in the interpretation of transient electromagnetic sounding data. Geophysics 59, 889–901.

Haber, E., Ascher, U.M., Oldenburg, D.W., 2004. Inversion of 3D electromagnetic data in frequency and time domain using an inexact all-at-once approach. Geophysics 69, 1216.

Hördt, A., Scholl, C., 2004. The effect of local distortions on time-domain electromagnetic measurements. Geophysics 68, 87–96.

Jacobsen, L.H., 2004, 1D-LCI-inversion of transient electromagnetic data, Master thesis, Department of Earth Sciences, University of Aarhus. Last seen February 2007 at http://www.gfs.au.dk/?id=195#Afhandlinger.

Jørgensen, F., Sandersen, P., Auken, E., 2003. Imaging buried Quaternary valleys using the transient electromagnetic method. Journal of Applied Geophysics 53, 199–213.

Meju, M.A., Fontes, S.L., Oliveira, M.F.B., Lima, J.P.R., Ulugergerli, E.U., Carrasquilla, A.A., 1999. Regional aquifer mapping using combined VES-TEM-AMT/EMAP methods in the semiarid eastern margin of Parnaiba Basin, Brazil. Geophysics 64, 337.

Munkholm, M.S., Auken, E., 1996. Electromagnetic noise contamination on transient electromagnetic soundings in culturally disturbed environments. Journal of Environmental & Engineering Geophysic 1, 119–127.

Newman, G.A., Anderson, W.L., Hohmann, G.W., 1987. Interpretation of transient electromagnetic soundings over three-dimensional structures for the central-loop configuration. Geophysical Journal Of The Royal Astronomical Society 89, 889–914.

Santos, F.A.M., 2004. 1-D laterally constrained inversion of EM34 profiling data. Journal of Applied Geophysics 56, 23–134.

Sørensen, K.I., Auken, E., 2004. SkyTEM — a new high-resolution helicopter transient electromagnetic system. Exploration Geophysics 35, 191–199.

Sugeng, F., 1998. Modelling the 3D TDEM response using the 3D full-domain finite-element method based on the hexahedral edge-element technique. Exploration Geophysics 615–619.

Tarantola, A., Valette, B., 1982. Generalized nonlinear inverse problems solved using a least squares criterion. Rewiews of Geophysics and Space Physics 20, 219–232.

Toft, M.W., 2001. Three-dimensional TEM modelling of near-surface resistivity variations, Masters Thesis, Department of Earth Sciences, University of Aarhus. At www.hgg.au.dk.

Wannamaker, P.E., Hohmann, G.W., SanFilipo, W.A., 1984. Electromagnetic modeling of three-dimensional bodies in layered earths using integral equations. Geophysics 49, 60–74.

Ward, S.H., Hohmann, G.W., 1988. Electromagnetic theory for geophysical applications. In: Nabighian, M.N. (Ed.), Electromagnetic Methods in Applied Geophysics. Society of exploration geophysicists (SEG), pp. 131–311.

Wisén, R., Christiansen, A.V., 2005. Laterally and mutually constrained inversion of surface wave seismic data and resistivity data. Journal of Environmental & Engineering Geophysics 10, 251–262.